ACS APPLIED NANO MATERIALS

www.acsanm.org Article

Structure and Optical Property Prediction of 2D Plasmonic Photonic Crystals Fabricated by Shadow Sphere Lithography

Yanfeng Wang, Dexian Ye,* Fengtong Zhao, Zhengjun Zhang,* and Yiping Zhao*

Cite This: *ACS Appl. Nano Mater.* 2022, 5, 17879−17890

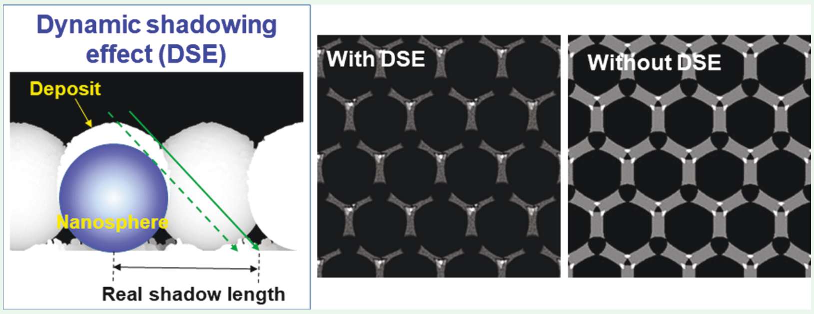

ABSTRACT: Shadow sphere lithography (SSL) is a powerful and large-scale fabrication method to produce two-dimensional (2D) plasmonic photonic crystals and three-dimensional metamaterials. Practically, one of the biggest challenges for SSL-based fabrications is that it is hard to accurately predict the physical properties of the fabricated nanostructures if the structures were only modeled by the geometric shadowing effect. A Monte Carlo (MC) simulation is developed to show that the dynamic shadowing effect due to the accumulation of materials on the template as well as the thin-film growth mechanism plays a key role in determining the structure details. For a one-to-three step-based SSL fabrication, the nanostructures predicted by MC match very well with those produced experimentally, and the plasmonic properties predicted by these MC-simulated structures are also consistent with the features obtained experimentally, both qualitative and semi-quantitative. This study indicates a possible solution to use MC simulation and numerical calculation to guide the design of the plasmonic photonic crystals and metamaterials based on SSL for optic applications.

KEYWORDS: *2D plasmonic photonic crystals, shadow sphere lithography, Monte Carlo simulation, plasmonics, optical property*

1. INTRODUCTION

Two-dimensional plasmonic photonic crystals (2D-PCCs), which can localize and enhance the electromagnetic fields and hence control the propagation of light, have attracted a lot of attention recently due to their widespread applications in photonics, such as planar optical components,[1] nonlinear optics,[2] super-resolution imaging,[3] optical trapping,[4] chemical and biological sensing,[5] and so forth. These applications require advanced, sophisticated, and scale-up fabrication techniques with a flexibility to control many material and structure parameters of 2D-PCCs. The most common fabrication strategies are conventional photolithography, electron-beam lithography, and/or ion-beam lithography.[6] These processes, however, are expensive and slow with limited access to research groups that need large-area 2D-PCCs. One convenient alternative to create periodic patterns is to use self-assembled colloidal monolayers as a template or a shadow mask and combine with deposition and/or etching to produce desired 2D-PCCs over a relatively large area (>1 cm^2). This method, which is commonly referred to as nanosphere lithography (NSL), when combined with oblique angle deposition [which is now referred to as shadow sphere lithography (SSL)], can produce a variety of 2D-PCCs and three-dimensional (3D) metamaterials.[1,7] As an inexpensive alternative to traditional lithography technologies, SSL can control the geometry of the shadow of the nanospheres in a variety of ways and provide the following advantages: (1) using nanospheres with different diameters, one can change the periodicity of the desired 2D-PCCs; (2) the shadow size can be controlled by the reduced size of the nanospheres via plasma etching,[8] as well as the deposition angle; (3) multi-angle depositions of one or more materials can achieve a large number of complex structures;[9] (4) the multiple large domains in the colloidal monolayer can be used to generate, in parallel, thousands of variations of structures for high-throughput

Received: August 30, 2022
Accepted: November 23, 2022
Published: December 6, 2022

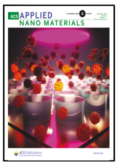

https://doi.org/10.1021/acsanm.2c03838

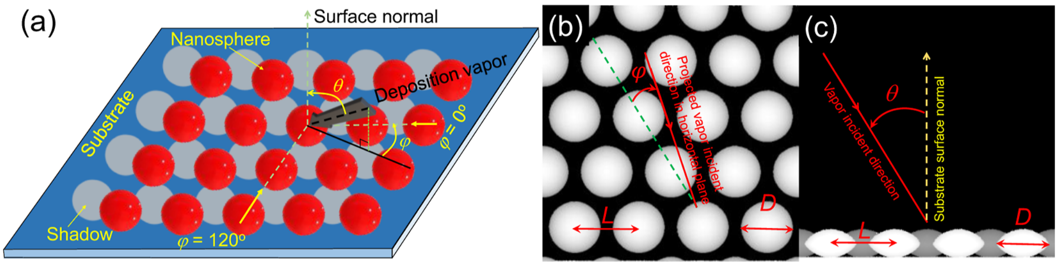

Figure 1. The schematic shows the definition of the detailed experimental and simulation parameters. (a) 3D view of the deposition and the definitions of θ and φ. (b) Definitions of nanosphere diameter D and azimuthal vapor incident angle φ. (c) Definition of lattice periodicity L and deposition angle θ.

screening of different 2D-PCCs which may produce unexpected optical response;[1] and (5) the nanosphere monolayer can be formed on a flexible substrate, and the symmetry of the monolayer can be modified by stretching the flexible substrate.[10] Clearly, SSL can produce an extensive variety of complex nanopatterns that have not previously been realized and can realize efficient prototyping and discovery of new 2D-PCCs.

Unlike the design of metasurfaces using the conventional lithography techniques, it is very hard to predict the optical properties of the 2D-PCCs made by SSL even though the overall structures can be predicted. In fact, several groups have established the numerical algorithms based on the geometric shadowing principle to predict the possible structure and shape of the resulting 2D-PCCs according to different fabrication conditions.[1,11,12] However, when these predicted nanostructures were used to forecast the optical response using a variety of numerical methods, such as finite-difference-time-domain (FDTD) method, finite element method, and so forth, there were significant differences between the forecasted results and the experimental results.[13−16] When the resulted 2D-PCCs only consist of one simple nanopattern, such as a nanotriangle array or a nanohole array, the numerically calculated optical properties could match fairly well with the experimental results.[17] However, if the nanostructure becomes more complicated, a large discrepancy appeared.[13−16] For example, the numerically calculated optical properties of the nanoparticle-in-ring array showed a resonance position 100 nm away from that of the experimentally obtained spectra,[14] while for various compound nanohole arrays, the predicted optical properties deviated significantly from the experimental results, and sometimes, they did not even show any similarity.[16] Thus, one could hardly use numerical calculations to estimate the optical properties of the proposed 2D-PCCs made by SSL and thus provide guidance for experiments. Such a discrepancy roots from the nanostructure prediction models: for all the SSL structure predicting models, they simply considered the geometrical shadowing of a moving deposition point source[9] but ignored the nonuniform material buildup on the nanospheres or substrates due to the shadowing and the subsequent shadowing effects, such as the narrowing of gaps between nanospheres, the extra shadowing effect due to material buildup (which we term it as dynamic shadowing effect), the diverging flux of the incident material from an uncollimated source, and the physical mechanisms that controlled the growth process, such as adatom moving, colliding, and coalescing along the surface due to the surface diffusion.[18] In addition, all the nanospheres in the templates are considered as perfect spheres regardless of whether or not they were plasma-etched. We will show later that during the plasma etching, the colloidal nanospheres change into a spheroid-like shape. Such a change could also alter the shadowing effect and produce structures different from those by perfect spheres in models reported in refs 111, and 12. All these effects produce the ultimate 2D-PCCs/metamaterials designed by SSL and could have structures or morphologies significantly deviate from the ideal nanostructures predicted by the geometric shadowing models. Such deviations exist not only in the shape of the structures but also in thickness distribution, roughness variation, and gaps among the individual unit structures. From the plasmonic property point-of-view, the change in shape, size, roughness, and gap could not only significantly alter the localized plasmonic properties (or the local electric fields) but also substantially change the electromagnetic coupling between adjacent nanostructures, thus introducing a significant discrepancy in optical property prediction. Therefore, a better strategy that is able to predict the details of the structure and morphology of the 2D-PCCs or metamaterials produced by SSL is of great important.

In this work, a three-dimensional Monte Carlo (3D MC) simulation method is developed to produce the detailed structure and morphology of the 2D-PCCs or metamaterials fabricated by SSL under different conditions. The MC model effectively considers the dynamic shadowing effect, the narrowing of gaps among nanospheres, the sticking and surface diffusion of adatoms during the deposition and can simultaneously predict the nonuniform distribution of deposition thickness, surface roughness, and additional shadowing effect during the multi-step growth process. Compared to the experimental 2D-PCCs obtained by scanning electron microscopy (SEM) or atomic force microscopy (AFM) under different conditions, the MC-produced nanostructures have a much higher similarity compared to those modeled by the pure shadowing effect. Based on the nanostructures predicted by MC, the optical properties are calculated by FDTD, and they are highly similar to the experimentally obtained spectra, as compared to those obtained from the shadowing effect only. Such results indicate that using 3D MC simulations and numerical calculations, one can better predict the optical properties of 2D-PCCs or metamaterials produced by SSL, which can provide an efficient, reliable, and useful guide to design 2D-PCCs or metamaterials fabricated by SSL for different optical applications.

https://doi.org/10.1021/acsanm.2c03838
ACS Appl. Nano Mater. 2022, 5, 17879−17890

2. EXPERIMENTAL SECTION AND SIMULATIONS

2.1. Experiments. This section gives a brief description of the experimental preparation procedure, and details can be found in previously published papers.[15−17,19,20] PS nanospheres of 750 nm diameter (Polyscience, Lot # 07107) were used to form the nanosphere monolayers onto cleaned glass slides (Gold Seal, Part # 3010). Ethanol (Sigma-Aldrich, 98%) was used for monolayer preparation. Glass substrates were cleaned in a boiling piranha solution (4:1 v/v of sulfuric acid/hydrogen peroxide) for at least 20 min. Sulfuric acid (Fisher Scientific, 98%) and hydrogen peroxide (Fisher Scientific, 30%) were used without further purification. After chemical cleaning, all substrates were thoroughly rinsed in DI water and dried with N_2 gas. Nanosphere monolayers with a domain size larger than 1×1 cm^2 were assembled on the clean glass substrates using an air/water interface technique as previously reported.[13,21] The diameter D of the nanospheres in the monolayer can be reduced to a desired D/L ratio via reactive ion etching to a preset etching time. The original or etched PNM-coated substrates were loaded on a substrate holder of a custom-built electron-beam deposition system where the polar angle θ (the angle between the substrate surface normal and the vapor deposition direction) and the azimuthal angle φ were controlled by two step motors (see Figure 1a). Ag nanopatterns were prepared according to the desired procedure to form different 2D-PCCs, that is, under different incident angles θ and azimuthal angles φ with a designed number of depositions. During all depositions, the deposition pressure was $<5 \times 10^{-6}$ Torr, the deposition rate was set to be 0.1 nm s^{-1}, and the Ag source was 99.999% pellets obtained from Kurt J Lesker Co. During each deposition step, the thickness t and the deposition rate were monitored in situ by a quartz crystal microbalance (QCM). In the above procedures, 18 MΩ•cm deionized (DI) water was used. For all the structures discussed later, the detailed deposition procedures are described in figure captions.

After deposition, the nanosphere monolayers were removed by Scotch tapes. The morphology of the resulting 2D-PCCs was characterized by a field-emission scanning electron microscope (FE-SEM, Zeiss GeminiSEM 500) and AFM (Park Systems NX-10 AFM). The optical properties were characterized using an ultraviolet−visible spectrophotometer (Perkin Elmer Lambda 35). The polarization-dependent spectra were achieved by adding a matched set of polarizers to the above spectrometer via a home-built mounting and alignment system.[19,20]

2.2. 3D MC Simulations. A full 3D MC simulator with a ballistic aggregation mechanism is developed for SSL under various conditions.[13,22,23] The simulation is based on a 3D cubic lattice with 720 lattice units in all the three dimensions, where the periodic boundary conditions are allowed in the in-plane directions. A cube with a unit size in the lattice is used to represent the depositing material [silver (Ag) atom in this case]. If the state of the cube is marked as unoccupied, the site associated is an empty space. When the state of the site changes from unoccupied to occupied, it means that a Ag particle has been deposited on the site. For all simulations, a planar surface with a thickness of 8 units was formed to serve as the substrate. A monolayer of the nanospheres with a radius of r units, arranged in a hexagonal pattern, was formed on the planar surface to mimic the templates used in SSL (Figure 1b). The period L of the nanospheres was fixed to be 240 units. The shape and diameter of the nanospheres were determined by the detailed SSL condition, that is, whether there were etching involved. If there was no etching, the monolayer was modeled as a hexagonal close-packed layer of perfect nanospheres with $r = L/2 = 120$. If a plasma etching step was involved, the 3D topology of the nanospheres was not a perfect sphere anymore, rather each etched nanosphere took a spheroid-like shape as shown in the side view image in Figure 1c, and the detailed etching time-dependent shape change was reported in ref 24. According to ref 24, the shape of the etched nanosphere can be treated as a combination of a top moving spheric cap and a stationary bottom spheric cap, with the diameter of the top spheric cap following $D(t) = \sqrt{L^2 - (kt)^2}$, where k can be treated as an effective etching rate. Such an empirical experimental result was used to model the etched nanosphere. For the shadowing deposition process, the Ag particles were generated at random positions around the monolayer template and allowed to move along a straight line trajectory at an impinging angle θ with respect to the surface normal direction, which is equivalent to the vapor incident angle θ used in the experiments. A ballistic sticking mechanism was used in the MC simulations, that is, a moving particle was deposited and added to the surface if any nearest-neighbor site was occupied by another cube along its trajectory. As soon as the depositing particle was settled on the surface, one of the previously deposited particles within a cube of $11 \times 11 \times 11$ units centered at the newly deposited particle was randomly selected for the random-walk-like surface diffusion process.[25] This diffusing particle searched its nearest neighbors for unoccupied sites and attempted to move one step from its current position. The move was successful if the new site could provide more bonding than the current one. Otherwise, the particle would stay at the present site. Whether or not the attempted move was successful, another particle would be chosen to repeat the diffusion process. This process would be continued until a fixed number N of the diffusing particles was selected and performed attempted diffusion. N is used to measure the diffusion strength of the material in the MC model and $N = 300$ was chosen for Ag in our simulations based on our previous testing of the MC model.[26] After finishing the diffusion process, a new particle was generated above the surface at a random position, and the deposition−diffusion sequence was repeated again and continuously until a total number of particles of 1.05×10^7 were deposited. The number of particles set in the simulation was used to represent the deposition time. In order to mimic the substrate azimuthal rotation, the trajectory of the incident particles was abruptly rotated azimuthally around the substrate normal, while θ was kept the same. After finishing the simulation, the monolayer template and the particle deposition on top of the templates were digitally removed to reveal the deposited 2D-PCCs on the substrates. The lateral and height distributions of the deposited structures on the substrate were rescaled to match the real size of the experimental nanospheres compared to the 2D-PCCs obtained experimentally under the same conditions and input into FDTD software for optical property calculations. Usually, it took about 20 min for one-step deposition to be finished.

2.3. MATLAB Prediction of 2D-PCCs. An in-house MATLAB program was used to numerically predict the 2D-PCC patterns formed on the substrate under different deposition conditions,[11] and now, it is available online.[12] This calculation predicted the pattern and thickness distribution of the Ag film on the substrate by considering the geometric shadowing effects from 36 nearby neighbors in a 2D hexagonal nanosphere array. Here, all the nanospheres, with or without plasma etching, are treated as perfect spheres, and the accumulations of materials on the surface of nanospheres and on the substrates are not considered in the calculation. This numerical calculation is referred to as "NC". Usually, these calculations took few minutes to finish.

2.4. FDTD Calculations. A commercial software package (FDTD Solutions, Lumerical Solutions Inc.) was used to calculate the plasmonic properties of the simulated Ag 2D-PCCs predicted by MC and NC. To compare the MC and NC results with the experimental results, the simulated/calculated 2D-PCCs were scaled laterally according to the periodicity L of the experimental hexagonal lattice. In the vertical direction, the average surface height of the predicted structures was adjusted carefully to be consistent to with the average experimental height of the corresponding structures obtained from SEM or AFM. The detail of the FDTD unit cell is shown in Section S1 of the Supporting Information. A rectangular unit cell was set as the calculation region with periodic boundary conditions in the two lateral dimensions. Perfectly matched layer boundary conditions were used on the top and bottom surfaces of the calculation domain. A "frequency domain field and power" monitor is set up to determine the transmission spectrum. The optical parameters for the Ag and glass (SiO_2) substrates were taken from Palik's handbook.[27]

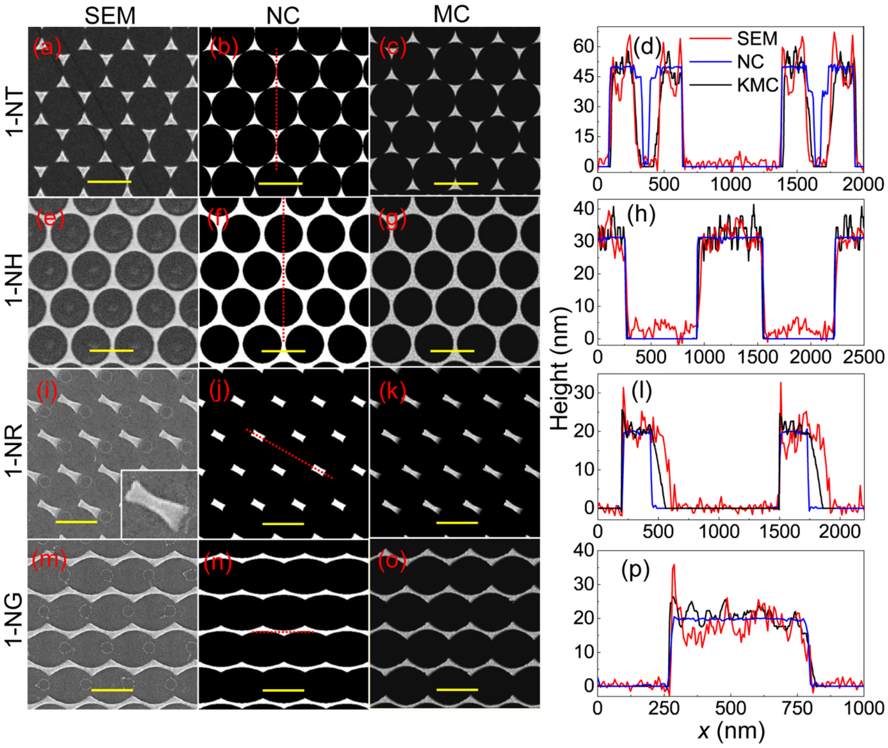

Figure 2. Some typical simple 2D-PCCs fabricated by one-step deposition of SSL on a L = 750 nm nanosphere monolayer: 1-NT structures produced under D = 750 nm and θ = 0°: (a) SEM, (b) NC, (c) MC, and (d) corresponding surface profiles along the dashed red line shown in (b); 1-NH structures fabricated under $D/L \approx 0.92$ and θ = 0°: (e) SEM, (f) NC, (g) MC, and (h) corresponding surface profiles along the dashed red line shown in (f); 1-NR structures demonstrated under $D/L \approx 0.889$, φ = 90°, and θ = 53°: (i) SEM (the inset shows the zoom-in figure of a single NR), (j) NC, (k) MC, and (l) corresponding surface profiles along the dashed red line shown in (j); 1-NG structures generated under $D/L \approx 0.889$, φ = 0°, and θ = 53°: (m) SEM, (n) NC, (o) MC, and (p) corresponding surface profiles along the dashed red line shown in (n). The scale bars in all images represent 750 nm. For all these depositions, the thickness t = 50 nm.

3. RESULTS AND DISCUSSION

3.1. Structure and Morphology Comparison. In order to demonstrate the superiority of the MC simulation in predicting SSL 2D-PCCs, first, the MC simulation and NC based on a geometrical shadowing model of basic structural units formed by one-step deposition of SSL were carried out and compared with the experimental morphologies.

3.1.1. 2D-PCCs Made by a Single Deposition. Figure 2 shows some typical Ag array structures that can be formed by a single deposition at different θ and φ based on SSL with the same nanosphere monolayer (with or without etching) as the template and the corresponding structures predicted by NC and MC, and the corresponding larger area SEM images can be found in Figure S2. These structures are the basic structural units that can be used to construct complex 2D-PCCs. In all these cases, the incident deposition flux is approximated as collimated beam, and ballistic (i.e., line-of-sight) shadowing prevents the incoming vapor from condensing into regions behind the nanospheres; shadowed regions are thus created where no growth occurs. The dimension of the shadow cast by the nanosphere rises rapidly with increasing deposition angle θ.[28]

Figure 2a−c shows a nanotriangle (1-NT) array formed by a vertical deposition on a close-packed nanosphere monolayer (no etching). Though all the figures show clear isolated and similar triangle structures, detailed inspection reveals that the apexes of the triangles from the experiment (SEM image in Figure 2a) are not as sharp as those predicted by NC and MC (Figure 2a,b). In fact, the surface profiles of these three structures plotted in Figure 2d show more differences: the apex-to-base length from NC is much larger than that from SEM and MC, while the apex-to-base length from SEM and MC is quite similar. Also, the profiles on top of the triangles are very smooth for NC, while for both SEM and MC, they fluctuate, demonstrating that roughness has been developed during the deposition. The fluctuations in SEM are larger than those in MC, and the dips on top of the nanotriangles from the SEM profile are due to the SEM charging effect (artifacts). Also notice that one cannot directly compare the roughness values obtained from SEM or AFM to those obtained from the rescaled images from MC since each lattice unit in MC does not represent an atom but rather an atomic cluster.

Figure 2e−g shows the nanohole (1-NH) array formation under a vertical deposition on a pre-etched nanosphere monolayer. After etching, the size D of the nanosphere was decreased, while the lattice period L remained unchanged. The circular shadowed area is isolated from each other, and the NH array is formed by the material deposited on the unshaded area. Figure 2e−g shows very similar circular arrays for SEM, NC, and MC, which are different from those observed for 1-NT. The surface profiles shown in Figure 2h only reveal one significant difference among these three figures: For structures predicted by NC, the deposited ridges are very smooth, while for SEM and MC, they are quite rough. The radii of nanospheres predicted by MC, SEM, and NC are very similar.

The nanorod (1-NR) array shown in Figure 2i−k demonstrates the most significant difference among SEM, NC, and MC. Most obviously, it appears that the thickness of

Table 1. Comparison of the Correlation Coefficient C_m of 2D-PCCs Observed in Experiments and Those Predicted by NC and MC

	NC and exp	MC and exp		NC and exp	MC and exp
1-NT	0.848 ± 0.004	0.892 ± 0.005	3-NTs	0.678 ± 0.005	0.75 ± 0.01
1-NH	0.925 ± 0.002	0.947 ± 0.005	3-NHs	0.874 ± 0.006	0.926 ± 0.002
1-NR	0.330 ± 0.005	0.637 ± 0.007	3-NRs	0.48 ± 0.02	0.49 ± 0.01
1-NG	0.67 ± 0.01	0.730 ± 0.007	3-NGs	0.45 ± 0.02	0.49 ± 0.02

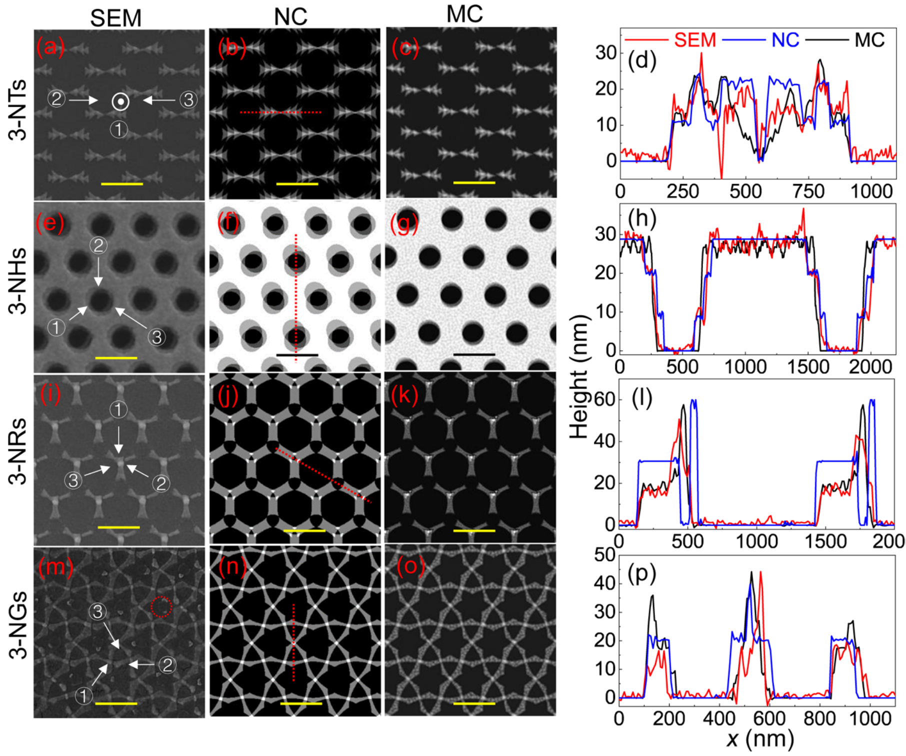

Figure 3. Some typical complex 2D-PCCs formed by the three-step deposition via SSL for L = 750 nm: 3-NTs fabricated or calculated under D = 750 nm, ① φ = 90°, θ = −15°, and t = 30 nm; ② θ = 0° and t = 30 nm; ③ φ = 90°, θ = 15°, and t = 30 nm: (a) SEM, (b) NC, (c) MC, and (d) corresponding surface profiles along the dashed red line shown in (b); 3-NHs produced under $D/L \approx 0.5$, ① φ = 0°, θ = 10°, and t = 20 nm; ② φ = 120°, θ = 20°, and t = 20 nm; ③ φ = 240°, θ = 30°, and t = 20 nm: (e) SEM, (f) NC, (g) MC, and (h) corresponding surface profiles along the dashed red line shown in (f); 3-NRs revealed under $D/L \approx 0.889$, ① φ = 90°, θ = 53°, and t = 30 nm; ② φ = 210°, θ = 53°, and t = 30 nm; ③ φ = 330°, θ = 53°, and t = 30 nm: (i) SEM, (j) NC, (k) MC, and (l) corresponding surface profiles along the dashed red line shown in (j); 3-NGs generated under $D/L \approx 0.889$, ① φ = 0°, θ = 53°, and t = 30 nm; ② φ = 120°, θ = 53°, and t = 30 nm; ③ φ = 240°, θ = 53°, and t = 30 nm: (m) SEM, (n) NC, (o) MC, and (p) corresponding surface profiles along the dashed red line shown in (n). The scale bars in all images represent 750 nm. The arrows and numbers in the first left column of the above figures show the projected φ-angles during deposition and the sequence of the three consecutive depositions.

the oblique deposited 1-NRs gradually becomes thinner from the top-left corner to the bottom-right corner as demonstrated by the zoom-in image in Figure 2i; that is, according to the trace left by the PS residue shown in Figure 2i (the small circles), the thicker part of the rod appears near the unshaded area between two adjacent nanospheres, while the thinner part resulted from under the bottom of the third nanosphere. The MC structure in Figure 2k shows similar thickness variation to those in the experimental one, while the NC structure in Figure 2j indicates uniform NRs with no thickness variation. Such differences are illustrated more clearly in surface profile plots shown in Figure 2l: first, the length of the NRs is very different, with the largest in SEM and the smallest predicted by NC. From the top-left corner to the bottom-right corner, the NC predicts two very steep boundaries, while for MC, there is a noninfinite height slope at the bottom-right corner. For SEM, the change in the bottom-right corner is even wider, with a similar slope to that of MC. Note that the big spikes in the SEM profile are due to the SEM artifacts. Also, the NC does not predict any roughness in the profile, while both SEM and MC show significant roughness variations on top of the rods. The nonuniform distributed thickness on the NRs for both SEM and MC could be due to the dynamic shadowing effect introduced during the deposition; that is, during the deposition, the thickness of the materials accumulated on the nanospheres gradually increases, resulting in a continuous shift of the shadowing starting position toward the top-left corner (see the later argument for multi-step deposition).

Finally, the nanograting (1-NG) arrays formed at θ = 53° and φ = 0° on a pre-etched nanosphere monolayer are shown in Figure 2m−o. Similar to the 1-NH structures shown in Figure 2e−g, the experimental structure and those predicted from NC and MC look quite similar in shape and dimension. Such a similarity in overall shape and dimension is also reflected by the surface profile plots in Figure 2p, and the only difference is that both SEM and MC show a significant roughness effect on the deposited NG, while there is only very small height variation in the NC predicted structure.

In order to obtain a more quantitative comparison among the structures predicted by MC and NC to the experimental structures, we calculated the correlation coefficients C_m of morphologies predicted by MC and NC with the experimental results according to ref 29. A monocell composed of individual deposited features was extracted from the image shown in Figure 2. To make a fair calculation, the monocells of the MC and NC images were carefully rescaled so that the lateral lengths of all the three cases were equal to the period L. The correlation coefficient of the matrix of the height distribution in different spatial positions in the monocells was calculated by the Corr2 function in MATLAB software. The definition of the Corr2 function is explained in Section S4 of the Supporting Information, and the C_m values for Figure 2 are summarized in the left side of Table 1. The C_m values between MC (column 3 in Figure 2) and SEM (column 1 in Figure 2) of the four structures are 0.892 ± 0.005, 0.947 ± 0.005, 0.637 ± 0.007, and 0.730 ± 0.007, respectively, while values between NC (column 2 in Figure 2) and SEM (column 1 in Figure 2) are 0.848 ± 0.004, 0.925 ± 0.002, 0.330 ± 0.005, and 0.67 ± 0.01, respectively, lower than the corresponding values between MC and SEM. The higher C_m values between MC and SEM indicate that the MC results can provide better structure predications for single-deposition SSL.

Clearly, for single-deposition 2D-PCCs formed via SSL, the MC predicts better structures than those from NC. The main shortcomings for NC predictions are two folds: first, it cannot predict the thin-film growth roughness due to far from equilibrium; second, it does not include the dynamic shadowing effect due to the growth of additional materials on the nanospheres. These two effects would become more significant if one considers 2D-PCC formations due to multiple depositions.

3.1.2. 2D-PCCs Made by Multi-deposition.

Figure 3 shows four complex 2D-PCCs that can be formed using triple depositions via SSL based on the structures formed in Figure 2 (the corresponding larger area SEM images can be found in Figure S2). The three overlapped triangle (3-NT) structures shown in Figure 3a−c are formed by changing the incident angle θ consecutively from −15° to 0° and then to +15°. The resulted individual 3-NT structure consists of a large triangle ($\theta = 0°$ deposition) in the center and two small triangles on two sides ($\theta = -15°$ and $\theta = +15°$ depositions). The top-view MC images of the structures formed after each step are shown in Figure S3a−b. Clearly, both MC and NC predict similar structures to those obtained by SEM. However, detailed inspection show that the two small triangles predicted by NC are of the same size, while from SEM and MC, the left small triangles resulting from $\theta = -15°$ deposition are a little larger than the right ones formed from $\theta = +15°$ deposition. A better illustration is shown in Figure S3d, where the nanotriangle arrays from the three consecutive depositions were decorated in different colors. Such a difference could be due to the dynamic shadowing effect since the $\theta = -15°$ deposition was the first step deposition, while the $\theta = +15°$ deposition was the third and final deposition. The surface profile plots show more significant differences. First, for 3-NTs predicted by NC, there are more height variations in the profile due to the overlap of the three triangles, but the height changes from one layer to another layer are quite steep (Figure 3d). However, the profiles from MC and SEM do not follow that from NC. They have many random variations, and the variations are not alike to each other.

The formation of the chiral nanohole (3-NH) array structure changes both the incident angle θ and the azimuthal angle φ together during three consecutive depositions,[15] and the corresponding structures are shown in Figure 3e−g. Apparently, they show quite different morphologies: the NC predicts largest hole shadows, followed by the SEM, and MC demonstrates the smallest shadows. The detailed structural similarity and difference can be seen from the surface profile plots (Figure 3h). The overall dimensions of the structures are quite similar for MC, SEM, and NC, which is consistent with the results shown in Figure 2h. However, the difference is quite significant. The NC predicts three clear layers in the edges of the holes, while such layered structures are not clear for MC and SEM. Also, there is roughness on the top deposited regions for these two cases.

The three stacked nanorod (3-NR) structures and three overlapped grating (3-NG) arrays are produced using a similar strategy based on the 1-NR and 1-NG method shown in Figure 2i−k, m−o: for three consecutive depositions, the azimuthal angle was changed from 0 to 120° and then to 240°. The 3-NR structures predicted by NC are quite different from those in MC and SEM: first, the three rods are identical in Figure 3j, and there is a small triangular hole among the three rods. In both SEM and MC results (Figure 3i,k), the three rods join together and are not identical. The width and length of the 3-NRs deposited successively in the plane gradually decreases with the increase of the deposition sequence. As the deposition direction (arrows) marked in Figure 3i, the longest and widest rod is the bottom rod marked by "1", followed by the left rod marked by "2", then finally the right NR marked by "3". A similar difference is observed for 3-NG structures shown in Figure 3m−o. The NC predicts identical nanograting in three azimuthal directions, while both MC and SEM show three different nanogratings: the width of the 3-NGs deposited successively gradually decreases with the increase of the deposition sequence as indicated by the numbered grating in Figure 3m. These observations are most possibly due to the dynamic shadowing effect during the deposition.

For a quantitative comparison, the C_m values have been calculated for the three-step deposition structures and are summarized in the right side of Table 1, the correlation coefficients for 3-NT, 3-NH, 3-NR, and 3-NG predicted by MC and SEM are 0.75 ± 0.01, 0.926 ± 0.002, 0.49 ± 0.01, and 0.49 ± 0.02, respectively. The corresponding C_m values between the NC predicated structures and SEM are lower, 0.678 ± 0.005, 0.874 ± 0.006, 0.48 ± 0.02, and 0.45 ± 0.02, respectively. Also, the corresponding C_m values are significantly smaller than those for 1-NT, 1-NH, 1-NR, and 1-NG. Such low C_m values may be due to two reasons. First, there are obvious traces of the PS residue in each original position of the PS nanospheres in the SEM images as shown by the dashed red circle in Figure 3m. A zoom-in image showing the PS residue is presented in Section S4 of the Supporting Information. The PS residuals change the height distribution of the area which should be flat and smooth, resulting in low C_m values. After digitally removing the PS residuals in the SEM image, the C_m value between NC and SEM for 3-NG is improved to 0.45 ± 0.02 while that between MC and SEM is increased to 0.49 ± 0.02. Second, the dynamic shadowing effect is more significant in the three-deposition situation than that in the one-deposition situation, which is reflected by the nonidentical triangles, rods, and grating shown in Figure 3a,i,m. To demonstrate the significance of the dynamic shadowing effect, we take the 3-NT fabrication as an example and examine how the deposit accumulated on the nanospheres would change the shadowing effect. Figure 4 shows the evolution of films deposited on top of the nanospheres via the top view and the cross-sectional view at the two deposition stages: halfway through the deposition and the final stage of deposition. The blue sphere in the cross-sectional view indicates the original nanosphere. Comparing Figure 4a,b, three notable differences can be seen: first, with more deposition, the top surfaces on the nanospheres become rougher, and the films tends to grow laterally to begin to fill out the voids among the nanospheres. Second, the thickness of the film on top of the nanosphere increases, that is, $h_1 < h_2$. Finally, for a collimated vapor with incident angle θ, the geometric shadowing length due to the deposited thin film becomes larger and larger with increasing deposition time, that is, $s_1 < s_2$. This phenomenon is also the cause of the nonuniform thickness distribution across the NRs in Figure 2i and can induce lateral growth on top of the nanospheres.[23] Such a dynamic shadowing effect depends not only on the film deposited onto the nanospheres but also on the symmetry of the lattice and the azimuthal rotation of the substrate.

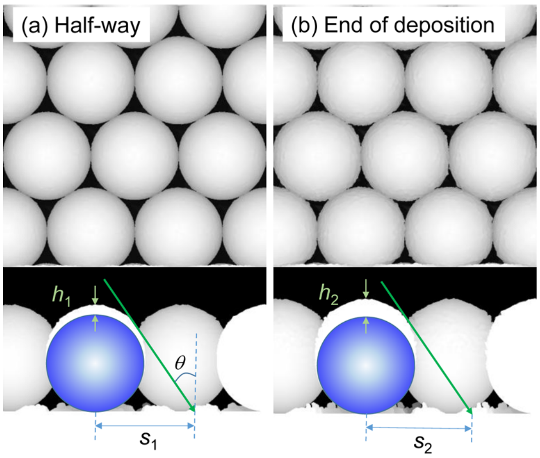

Figure 4. Top-view and cross-sectional view of films deposited onto the nanospheres for the 3-NT fabrication process: (a) half-way through deposition and (b) at the end of the deposition. The blue sphere indicates the location of the original nanosphere on the substrate. The green arrow shows the vapor deposition direction, h_1 or h_2 indicates the thickness of the film on top of the nanosphere, while s_1 or s_2 is the vapor shadow length.

3.2. Optical Property Prediction and Comparison.

The accuracy in the structure and morphology prediction for 2D-PCCs made by SSL can greatly influence the prediction for their optical properties. Comparison between the MC simulation morphologies and the experimental structures is a direct proof of the ability of using MC to better simulate the structural morphologies of SSL. Many previous studies on 2D-PCCs produced by SSL only reported the experimentally determined optical properties, and the prediction of the corresponding optical properties is either qualitative or semi-quantitative. Even when one used FDTD or other advanced numerical calculation methods, only the calculations on very simple structures such as those shown in Figure 2 can match the experimental results well. For example, Lee et al. fabricated Ag 1-NH structures and found that their optical properties matched well with FDTD calculations.[30] We also compared the experimental results and calculations of optical properties of Ag 1-NH[31] and even oval NH,[17] they were quite consistent. However, sometimes, even for 1-NT structures, the numerically predicted optical properties do not agree with the experimental results. For example, in Van Duyne's group, the predicted plasmonic properties of Cu and Al 1-NTs, though follow the trend for thickness and material dependence, deviated significantly from the experimental results.[32] For more complex structures, the calculations based on NC-predicted structures are quite different from the experiments. In the previous section, we demonstrate that the MC can better predict the 2D-PCC structures under different deposition conditions, and it is expected that in terms of optical property prediction, the electromagnetic calculations based on the structures predicted by MC should match the experimental results better. As an example, a complex 2D-PCC, the nanograting and nanohole structure (NG-NH), fabricated by two-deposition SSL, was experimentally prepared, and the polarization angle-dependent transmission spectrum $T(\lambda,\phi)$ was characterized. Similar to the deposition azimuthal angle φ defined in Figure 1a, the polarization angle ϕ for optical measurements is defined as the angle formed by the projected electric field direction of the linear polarized light and the long axis direction of the NG. Figure 5a−c shows the morphologies of the structure obtained experimentally, predicted by NC and MC, respectively (see Figure S2h for a larger area SEM image). The overall NG-NH structures presented in these three mages are very similar: in each hole, the nanograting introduces two spikes, one on top and the other at the bottom of the hole; the overlap of the nanograting and the ridge of the hole produces higher surface features along the horizontal direction (small white spots in the images). However, the SEM image shows that there are gaps between the top and bottom nanograting and hole, while NC predicts none. However, in the structure predicted by MC, the gaps exist. The surface profile plots in Figure 5d further illustrate such a difference: for the structure predicted by NC, there is a height spike at the interface between the nanograting and the hole, while for SEM and MC, this is a dip. Also, both SEM and MC show surface roughness on the ridge, while none in the structure was predicted by NC. However, the overall dimension of the three structures is similar. The C_m value between MC and experimental structure is 0.85 ± 0.01, while for NC, $C_m = 0.76 \pm 0.01$, which is slightly less.

Though the structures among the experiment, NC, and MC are much alike, the optical transmission spectra $T(\lambda,\phi)$ obtained from the experiments and predicted by FDTD, as shown in Figure 5e−g, are quite different (the detailed explanations of the peaks and dips in the spectra can be found in ref 20). Due to the deposition of the nanograting array, the structure becomes anisotropic and shows a strong polarization-dependent optical response as shown by Figure 5e: the $T(\lambda, 0°)$ shows a broad transmission peak shape at $\lambda_p = 1025$ nm, which is due to the enhanced optical transmission of NH arrays;[20,33] when ϕ increases, in the 700−1300 nm wavelength range, the transmission decreases and the spectral shape changes significantly, while in the 1300−2500 nm range, the transmission increases. As shown in $T(\lambda, 90°)$, three dips are formed as indicated by the dashed lines in Figure 5e, with $\lambda_{D1} = 956$, $\lambda_{D2} = 1054$, and $\lambda_{D3} = 1175$ nm, respectively. The dip at λ_{D1} is a result of Wood's anomaly.[34] The small Fano-like dips

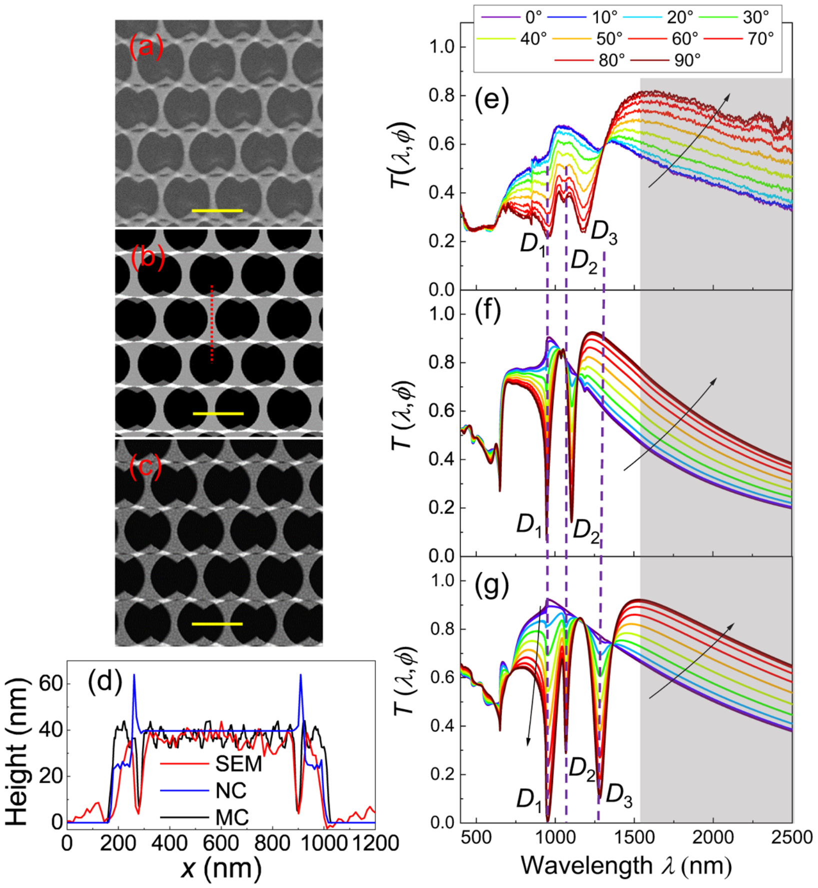

Figure 5. Nanograting on the nanohole structure formed by a two-step deposition via SSL. The deposition and calculation condition are $L = 750$ nm, $D/L \approx 0.861$, ① $\varphi = 0°$, $\theta = 53°$, and $t = 10$ nm; ② $\theta = 0°$ and $t = 10$ nm; and repeating ① and ② five times. Structures revealed by (a) SEM, (b) NC, (c) MC, and (d) surface profiles along the dashed red line shown in (b). Corresponding polarization-dependent transmission spectrum $T(\lambda,\phi)$ of the structure: (e) Experimental $T(\lambda,\phi)$ and FDTD-calculated $T(\lambda,\phi)$ based on the structures predicted by (f) NC and (g) MC. The arrows in the spectral plots show the spectral trend with increasing ϕ. The scale bars in all the images represent 750 nm.

at λ_{D2} and λ_{D3} are due to the destructive interference of the higher order resonances of NGonNH (octupolar mode and hexapole mode for D_2 and D_3) with the overlapping EOT peak.[33] The detailed physical explanation of the peak and dips can be found in ref 20. The FDTD calculated $T(\lambda,\phi)$ based on the structures predicted by NC (Figure 5f) shows an overall similar trend with the change of ϕ; that is, $T(\lambda, 0°)$ has a broad absorption peak, and when ϕ increases, in the 700−1140 nm wavelength range, the transmission decreases, and only two sharp dips at $\lambda_{D1} = 946$ and $\lambda_{D2} = 1108$ nm begin to evolve, while the transmission in the 1200−2500 nm range increases with a large decreasing slope compared to those in Figure 5e. For the $T(\lambda,\phi)$ calculated based on the structures predicted by MC (Figure 5g), the peak for $T(\lambda, 0°)$ appear at $\lambda_p = 961$ nm, and three dips are formed in $T(\lambda, 90°)$, with $\lambda_{D1} = 952$, $\lambda_{D2} = 1072$, and $\lambda_{D3} = 1285$ nm, respectively. Except for λ_{D3}, both λ_{D1} and λ_{D2} are quite close to the experimentally obtained values as indicated by the purple dashed lines through the spectral figures. The decreasing spectral shape in the wavelength 1600−2500 nm range is also quite like those in the experimental spectra. Apparently, $T(\lambda,\phi)$ calculated based on the MC structure can better reflect the experimental spectra. A more quantitative comparison is to calculate the correlation coefficient C_o of $T(\lambda,\phi)$ between the experiments and calculations from different origins. The results for $T(\lambda, 0°)$ and $T(\lambda, 90°)$ are summarized in Table 2. Though the morphological C_m values for structures predicted by MC (0.85 ± 0.01) and NC (0.76 ± 0.01) are quite similar, the C_o values for $T(\lambda, 0°)$ and $T(\lambda, 90°)$ are significantly different: The C_o values from MC structures are all >0.5, close to the C_m value of the morphology of MC simulation, while the C_o values from NC structures changes a lot; especially for $T(\lambda, 90°)$, the C_o value is even smaller than 0.1. Such a result indicates that the minute difference in structure prediction caused by the dynamic shadowing effect can introduce a big difference in optical property prediction since in plasmonics, the detailed local structure is very important. The discrepancy in C_m and C_o values for MC structures could be due to various reasons such as detailed roughness and height variations shown in Figure 5d, the accuracy of the MC model, and the use of the dielectric function for Ag in FDTD calculation since the experimental thin films could introduce more loss compared to those of the bulk Ag. Nevertheless, the above results clearly demonstrate that more accurate prediction of the structures ensures that the

Table 2. Comparison of the Correlation Coefficient C_o of the Transmission Spectrum $T(\lambda,\phi)$

ϕ	MC and exp	NC and exp
0°	0.7834	0.5929
90°	0.6540	0.0696

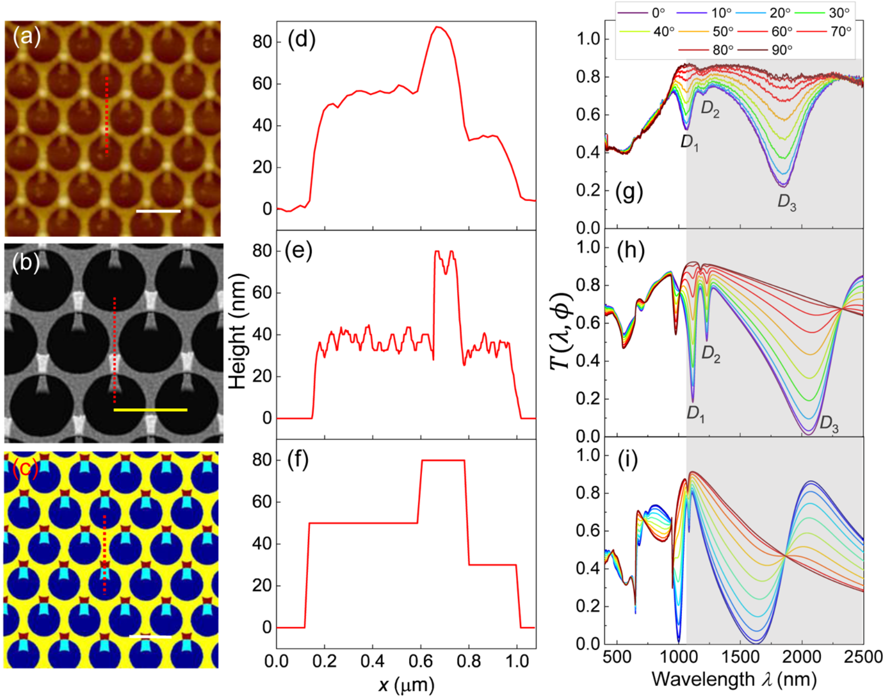

Figure 6. Connected NH-NR structure fabricated by a two-step SSL using an etched nanosphere monolayer under the following conditions: $D/L \approx 0.861$: ① $\theta = 53°$, $\varphi = 30°$, and $t = 50$ nm; ② $\theta = 0°$ and $t = 50$ nm. (a) Typical AFM image of the resulting structure; (b,c) structures predicted by MC and NC; (d–f) corresponding surface profile plot along the red lines in images; and (g–i) corresponding $T(\lambda,\phi)$ measured experimentally or calculated by FDTD using predicted structures. The scale bars in all images represent 750 nm.

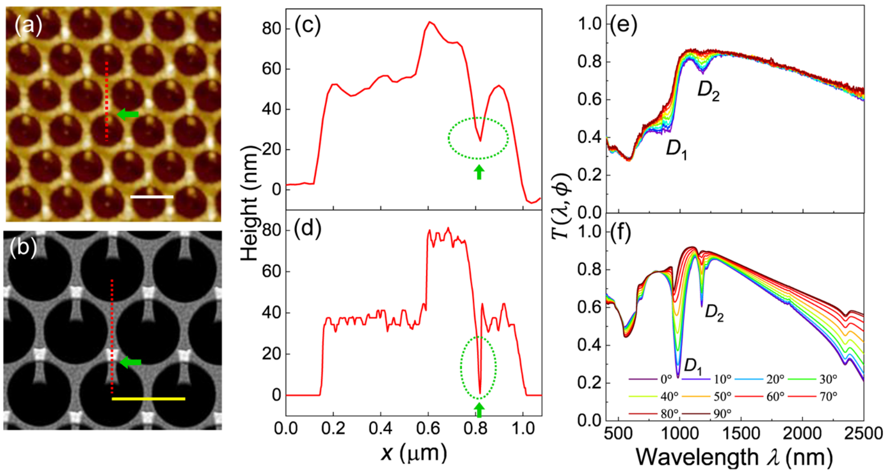

Figure 7. Disconnected NH-NR structure fabricated by a two-step SSL using an etched nanosphere monolayer under the following conditions: $D/L \approx 0.861$: ①$\theta = 0°$ and $t = 50$ nm; ②$\theta = 53°$, $\varphi = 30°$, and $t = 50$ nm. (a) Typical AFM image of the resulting structure; (b) structure predicted by MC; (c,d) corresponding surface profile plot along the red lines in images; and (e,f) corresponding $T(\lambda,\phi)$ measured experimentally or calculated by FDTD using the MC-predicted structure. The scale bars in all images represent 750 nm.

calculated optical properties can better match the real experimental results.

In multi-step SSL, the dynamic shadowing effect can not only change the detailed morphology of the 2D-PCCs but also influence the detailed structures when there is a change in the deposition sequence; therefore, the optical property can be adjusted. As an example, below we will show how the fabrication sequence could affect the formation of the nanorod-in-nanohole (NH-NR) array using a two-step SSL.[19] The NH-NR structures were fabricated by first depositing 50 nm Ag at $\theta = 53°$ and $\varphi = 30°$ for the etched nanosphere array with $D/L \approx 0.861$. Such a deposition formed the 1-NR array as shown in Figure 2i. Then, another 50 nm Ag was deposited at $\theta = 0°$ to form the NH array. A typical AFM image is shown in Figure 6a which clearly indicates that in every NH, there is a NR on top. However, the nanoholes are not perfect circles; they are slightly distorted to be an oval shape. This is caused by the dynamic shadowing effect in the second deposition step: During the oblique deposition of the first NR structure (first step), Ag is gradually accumulated on top of the nanospheres and formed an asymmetric spherical crown. At the follow-up NH deposition at $\theta = 0°$, the projections of nanospheres are no longer circular; instead, they are oval in shape. The structures predicted by MC (Figures 6b) further confirm such a shape change while the NC cannot (Figures 6c). The AFM profile in Figure 6d shows that the thickness of NH is about 50 nm, while the thickness of NR is about 30 nm. This result is consistent with the deposition configuration: for NH deposition, $\theta = 0°$, and the deposited Ag thickness should be the same as that monitored by QCM (50 nm), while for NR deposition, the deposition angle was $\theta = 53°$ and the effective thickness should be 50 nm × cos53° = 30 nm. For the MC, 50 nm thickness was used for both NR and NH features, and there is not two-stair feature in Figure 6e, compared to those in Figure 6d,f (NC). The C_m value between MC (Figure 6b) and AFM (Figure 6a) is 0.801 ± 0.009, while for NC (Figure 6c) and AFM (Figure 6a), it is $C_m = 0.695 \pm 0.007$, lower than the corresponding values between MC and AFM. The higher C_m between MC and AFM indicates that the MC results can provide better structure predications for single-deposition-based SSL. The similarity among the surface profiles shown in Figure 6d−f also supports the high C_m values.

However, if the order of the two steps is reversed, SSL would produce a lightly different structure. Figure 7a shows the representative AFM image of the NH-NR structures formed by first depositing 50 nm Ag at $\theta = 0°$ to form the NH array and then depositing the other 50 nm Ag at $\theta = 53°$ and $\varphi = 30°$ to form NR inside NH (see Figure S2i for a larger area SEM image). Though the overall morphology of Figure 7a is similar to that of Figure 6a, the surface profile shows significant difference as demonstrated in Figure 7c; that is, at around $x = 0.8$ μm, there is a dip as marked by the green arrow in Figure 7a,c. Such a dip corresponds a gap between the NR and the NH, indicating that the NR and NH are not connected. The structure (Figure 7b) predicted by MC further confirms such a morphology (NC cannot predict the disconnected NH-NR structure). In the surface profile plot, there is also a sharp dip at around $x = 0.8$ μm. Such a disconnection between NR and NH is caused by the dynamic shadowing effect, that is, for the second deposition, the 50 nm-thick NH deposited first can build a small shielding area at the edge of the NH, where vapors cannot reach during the second deposition. However, for Figure 6a, the second deposition of NH is not an oblique deposition, and NR deposited on the substrate in the first step will not produce any self-shadowing effect on the subsequent deposition of NH. Therefore, the NH structure can be superimposed on the NR structure very well, forming a connected NH-NR structure. The C_m value between MC (Figure 7b) and AFM (Figure 7a) is 0.83 ± 0.01, while $C_m = 0.754 \pm 0.006$ between the NC (Figure 6c) and the AFM (Figure 7a), slightly lower than the corresponding values between MC and AFM.

Though the structures are slightly different due to the change of the deposition order, the experimental optical spectra $T(\lambda,\phi)$ are significantly different. Here, the polarization angle ϕ for optical measurements is defined as the angle formed by the projected electric field direction of the linear polarized light and the long axis direction of the NR. As shown in Figure 6g, the experimental spectra show very strong polarization dependence for connected NH-NR, while for the disconnected NH-NR structures, there is only slight polarization dependence as shown in Figure 7e, in particular, in the 730−1330 nm wavelength range. The $T(\lambda, 90°)$ spectrum (Figure 6g) for the connected NH-NR structure shows a very broad (almost invariant) transmittance at $\lambda > 1000$ nm, which is quite similar to that for the disconnected NH-NR structure shown in Figure 7e. However, the $T(\lambda, 0°)$ spectrum (Figure 6g) for the connected NH-NR structure exhibits three distinct dips, with $\lambda_{D1} = 1062$, $\lambda_{D2} = 1197$, and $\lambda_{D3} = 1848$ nm, respectively, while the one (Figure 7e) for disconnected NH-NR structure shows two small dips at $\lambda_{D1} = 923$ and $\lambda_{D2} = 1183$ nm. The explanation of these dips from plasmonics perspective can be found in ref 19. Again, the result demonstrates that the minute changes due to the dynamic shadowing effect can significantly alter the plasmonic response.

In addition, comparing the $T(\lambda,\phi)$ obtained experimentally and those calculated by FDTD based on the predicted structures, the MC structures give a better match. For the connected NH-NR structure, the FDTD calculated $T(\lambda, 90°)$ spectrum (Figure 6h) from MC shows a broad slow varying transmission in the $\lambda > 1000$ nm wavelength range, which is pretty consistent with the experimental spectrum, while the $T(\lambda, 0°)$ spectrum exhibits three dips at $\lambda_{D1} = 1117$, $\lambda_{D2} = 1232$, and $\lambda_{D3} = 2060$ nm, respectively. These dip locations are close to the dip locations observed experimentally. However, the $T(\lambda,\phi)$ spectra predicted by NC structures (Figure 6i) are very different from the experimental ones. Similarly, for the disconnected NH-NR structures, the $T(\lambda, 0°)$ spectrum based on the MC structure predicts two dips at $\lambda_{D1} = 981$ and $\lambda_{D2} = 1185$ nm, which are very close to those demonstrated in the experiment. The correlation coefficient C_m and C_o comparison is discussed in Section S6 of SI, which further confirms the above conclusions.

Though through Figures 5−7, the optical properties predicted via the MC structures can better match the experimental results, the predictions are far from perfect (mostly $C_o < 0.8$). There are a few factors that could contribute to these mismatches: The first is due to MC simulation. The MC simulation was conducted in a 720 × 720 × 720 cubic lattice, the nanosphere took a diameter of 240 units in the entire lattice space, and each deposited particle occupied 1 unit. Then, the final nanosphere diameter was rescaled to 750 nm. Thus, one could not treat the depositing particle as a single atom. Effectively, each deposition particle in MC should correspond to a cubic cluster, with a size 3.1 nm × 3.1 nm × 3.1 nm, which itself would introduce an artificial roughness of around 3 nm. Therefore, a lot of microscale details are still missing in the MC structures. Also, in one MC, only 8 units of nanospheres were simulated, while in experimental measurements, if the optical beam diameter is about 1 mm, at least 10^6 nanostructures are probed. Therefore, there could be no enough statistics in the calculations based on MC structures. Second, since experimental measurement probes a much larger area, there are always defects in the sampling areas as shown in Figure S2 of SI. Thus, the quality of the nanosphere monolayer could contribute significantly to the mismatch. Finally, the dielectric functions used for the calculations are coming from the published data. For the resulting Ag films, the quality (such as crystallinity, defect, etc.) could be different, and there is a deviation between the real dielectric function and those from the literature. The latter two issues can be taken care of if better experimental conditions can be implemented, while for issues related to MC, two solutions are suggested: The first is to use a larger lattice to exactly match the atomic dimension of the nanostructures. Such a method requires a lot of computing power and is time-consuming, especially if statistics is needed. The second strategy is combining the MC simulation and thin-film roughness evolution laws to make simulated nanostructures.

It is well known that during thin-film growth, the roughness and lateral dimension of the microstructures can follow the so-called dynamic scaling rules.[35] One can experimentally determine these dynamic rules and use numerical methods to simulate the surface morphologies due to specific dynamic scaling laws.[35,36] These roughness morphologies can be added to the MC simulated structures to achieve better 2D-PCC structures for optical property calculations.

4. CONCLUSIONS

In summary, during the 2D-PCC fabrication process by SSL, the dynamic shadowing effect caused by the accumulation of materials on the template (nanosphere arrays) plays a vital role in determining the detailed structural morphology. It not only slightly changes the size and shape of the resulting nanostructures but also introduces different shadowing effects, and even the deposition sequence for multi-step fabrication can change the detailed structural morphology (or even break the symmetry). In addition, the roughness generated by thin-film deposition also plays an important role in determining the final morphology. The comparison of various experimental nanostructures and simulated/calculated nanostructures by 1–3 step deposition(s) via SSL shows that the MC model can better predict the structural details than the numerical model (NC) that only considers the self-shadowing effect. Since the plasmonic property depends closely on the detailed structural parameters, the optical properties calculated by FDTD from MC nanostructures can match the experimental spectra very well, whereas the calculations based on the NC model produce big discrepancies. Our study clearly reveals the following important issues for SSL: First, to use SSL to design desired 2D-PCCs or metamaterials is not trivial since the detailed structures would be governed by the dynamic shadowing effect and the film growth mechanism. If these two effects are ignored, the resulting nanostructure may produce properties that are not expected. Second, by carefully designing the deposition strategy, the effect of dynamic shadowing can be minimized. For example, in our previous work to prepare large-area NH-NR structures, we use multiple steps of thinner film depositions to avoid the significant dynamic shadowing effect,[19] that is, if the final NR and NH thickness is 50 nm, we only deposit 10 nm of each in one round and carry five rounds of two-step depositions, so that we can achieve a better structure control. Third, the dynamic shadowing effect can be used to design some desired nanostructures. For example, by controlling the deposition on top of the nanospheres, one could design particle-in-ring structures,[14] or one can also continuously tune the nanostructures from discrete nanopatches to continuum nanohole films,[23] or one can make connected and disconnected NH-NR structures shown in Figures 6 and 7. Finally, practically, one of the biggest challenges for SSL-based fabrications is that the physical properties of the resulting or designed nanostructures can hardly be predicted. This work indicates that the combination of the MC simulation and numerical methods for property prediction is a possible solution, which paves a way to use simulation and numerical calculation to guide the design of the 2D-PCCs or metamaterials based on SSL. However, though the MC can predict better structural details, the matches between the experimental results and the predicted nanostructures are not perfect (mostly $C_m < 0.85$), and the predicted optical properties cannot exactly match with the experimental results, which demonstrates that the MC model needs further improvement, and more realistic optical dielectric functions should be used.

Since SSL is a very versatile fabrication technology for 2D-PCCs and metamaterials, this study can help people to better predict the optical properties of the resulting nanostructures and could impact greatly their optical applications.

■ ASSOCIATED CONTENT

Supporting Information

The Supporting Information is available free of charge at https://pubs.acs.org/doi/10.1021/acsanm.2c03838.

> General lattice setup for FDTD calculation; zoom-out SEM images for structures shown in Figures 2, 3, 5, and 6; illustration of consecutive nanotriangle formation in the 3-NT structure; definition of Corr2 in MATLAB; zoom-in SEM image to show the PS residue in the 3-NG structure; and comparison of the correlation coefficient of transmission spectra for connected NH-NR and disconnected NH-NR structures (PDF)

■ AUTHOR INFORMATION

Corresponding Authors

Dexian Ye – *Department of Physics, Virginia Commonwealth University, Richmond, Virginia 23284, United States;* orcid.org/0000-0002-1104-2463; Email: dye2@vcu.edu

Zhengjun Zhang – *Key Laboratory of Advanced Materials (MOE) and School of Materials Science and Engineering, Tsinghua University, Beijing 100084, P. R. China;* orcid.org/0000-0001-8727-6373; Email: zjzhang@tsinghua.edu.cn

Yiping Zhao – *Department of Physics and Astronomy, University of Georgia, Athens, Georgia 30602, United States;* orcid.org/0000-0002-3710-4159; Email: zhaoy@uga.edu

Authors

Yanfeng Wang – *Key Laboratory of Advanced Materials (MOE) and School of Materials Science and Engineering, Tsinghua University, Beijing 100084, P. R. China; Department of Physics and Astronomy, University of Georgia, Athens, Georgia 30602, United States;* orcid.org/0000-0001-7698-6230

Fengtong Zhao – *Key Laboratory of Advanced Materials (MOE) and School of Materials Science and Engineering, Tsinghua University, Beijing 100084, P. R. China*

Complete contact information is available at: https://pubs.acs.org/10.1021/acsanm.2c03838

Author Contributions

Y.F.W. and F.G.Z. performed the experiments, structure characterization, and data analysis. D.X.Y. carried out MC simulations and data analysis. Z.J.Z. and Y.P.Z. contributed to the concepts of the manuscript and fund acquisitions. All authors contributed to the manuscript writing. All authors have given approval to the final version of the manuscript.

Notes

The authors declare no competing financial interest.

■ ACKNOWLEDGMENTS

YFW, FGZ, and ZJZ were supported by the Basic Science Centre Project of NSFC under grant no. 51788104. YPZ was supported by the National Science Foundation under grant no. ECCS-1808271.

■ REFERENCES

(1) Nemiroski, A.; Gonidec, M.; Fox, J. M.; Jean-Remy, P.; Turnage, E.; Whitesides, G. M. Engineering Shadows to Fabricate Optical Metasurfaces. *ACS Nano* **2014**, *8*, 11061−11070.

(2) Melentiev, P. N.; Afanasiev, A. E.; Kuzin, A. A.; Gusev, V. M.; Kompanets, O. N.; Esenaliev, R. O.; Balykin, V. I. Split Hole Resonator: A Nanoscale UV Light Source. *Nano Lett.* **2016**, *16*, 1138−1142.

(3) Cao, S.; Wang, T.; Sun, Q.; Hu, B.; Yu, W. Meta-nanocavity model for dynamic super-resolution fluorescent imaging based on the plasmonic structure illumination microscopy method. *Opt. Express* **2017**, *25*, 3863−3874.

(4) (a) Zhou, S.; Yang, Z.; Gao, P.; Li, X.; Yang, X.; Wang, D.; He, J.; Ying, Z.; Ye, J. Wafer-Scale Integration of Inverted Nanopyramid Arrays for Advanced Light Trapping in Crystalline Silicon Thin Film Solar Cells. *Nanoscale Res. Lett.* **2016**, *11*, 194. (b) Zhan, Y.; Wang, Y.; Cheng, Q.; Li, C.; Li, K.; Li, H.; Peng, J.; Lu, B.; Wang, Y.; Song, Y.; Jiang, L.; Li, M. A Butterfly-Inspired Hierarchical Light-Trapping Structure towards a High-Performance Polarization-Sensitive Perovskite Photodetector. *Angew Chem Int Ed Engl* **2019**, *58*, 16456−16462.

(5) Song, C.; Jiang, X.; Yang, Y.; Zhang, J.; Larson, S.; Zhao, Y.; Wang, L. High-Sensitive Assay of Nucleic Acid Using Tetrahedral DNA Probes and DNA Concatamers with a Surface-Enhanced Raman Scattering/Surface Plasmon Resonance Dual-Mode Biosensor Based on a Silver Nanorod-Covered Silver Nanohole Array. *ACS Appl. Mater. Interfaces* **2020**, *12*, 31242−31254.

(6) Su, V.-C.; Chu, C. H.; Sun, G.; Tsai, D. P. Advances in optical metasurfaces: fabrication and applications [Invited]. *Opt. Express* **2018**, *26*, 13148−13182.

(7) Ai, B.; Zhao, Y. Glancing angle deposition meets colloidal lithography: a new evolution in the design of nanostructures. *Nanophotonics* **2018**, *8*, 1−26.

(8) Yan, W. G.; Kong, X. T.; Li, Z. B.; Tian, J. G. Nanostructure fabricated by nanosphere lithography assisted with O2 plasma treatment. *J. Nanosci. Nanotechnol.* **2013**, *13*, 4311−4315.

(9) (a) Myint, B.; Yap, D. S. F.; Ng, V. Stepwise nanosphere lithography: an alternate way of fabricating nanostructures. *Nano Express* **2020**, *1*, 020029. (b) Kosiorek, A.; Kandulski, W.; Chudzinski, P.; Kempa, K.; Giersig, M. Shadow Nanosphere Lithography: Simulation and Experiment. *Nano Lett.* **2004**, *4*, 1359−1363.

(10) Vogel, N.; Weiss, C. K.; Landfester, K. From soft to hard: the generation of functional and complex colloidal monolayers for nanolithography. *Soft Matter* **2012**, *8*, 4044−4061.

(11) Larsen, G. K.; He, Y.; Ingram, W.; Zhao, Y. Hidden Chirality in Superficially Racemic Patchy Silver Films. *Nano Lett.* **2013**, *13*, 6228−6232.

(12) Bradley, L.; Lin, X.; Chen, Y.; Asadinamin, M.; Ai, B.; Zhao, Y. Janus Particles with Flower-like Patches Prepared by Shadow Sphere Lithography. *Langmuir* **2021**, *37*, 13637−13644.

(13) Ingram, W.; He, Y.; Stone, K.; Dennis, W. M.; Ye, D.; Zhao, Y. Tuning the plasmonic properties of silver nanopatterns fabricated by shadow nanosphere lithography. *Nanotechnology* **2016**, *27*, 385301.

(14) Ai, B.; Song, C.; Bradley, L.; Zhao, Y. Strong Fano Resonance Excited in an Array of Nanoparticle-in-Ring Nanostructures for Dual Plasmonic Sensor Applications. *J. Phys. Chem. C* **2018**, *122*, 20935−20944.

(15) Ai, B.; Luong, H. M.; Zhao, Y. Chiral nanohole arrays. *Nanoscale* **2020**, *12*, 2479−2491.

(16) Skehan, C.; Ai, B.; Larson, S. R.; Stone, K. M.; Dennis, W. M.; Zhao, Y. Plasmonic and SERS performances of compound nanohole arrays fabricated by shadow sphere lithography. *Nanotechnology* **2018**, *29*, 095301.

(17) Ai, B.; Basnet, P.; Larson, S.; Ingram, W.; Zhao, Y. Plasmonic sensor with high figure of merit based on differential polarization spectra of elliptical nanohole array. *Nanoscale* **2017**, *9*, 14710−14721.

(18) Pimpinelli, A.; Villain, J.*Physics of Crystal Growth*; Cambridge University Press, 1998.

(19) Wang, Y.; Chong, H. B.; Zhang, Z.; Zhao, Y. Large-Area Fabrication of Complex Nanohole Arrays with Highly Tunable Plasmonic Properties. *ACS Appl. Mater. Interfaces* **2020**, *12*, 37435−37443.

(20) Wang, Y.; Choi, I.; Zhang, K.; Yang, Y.; Ao, S.; Xue, X.; Fu, W.; Zhang, Z.; Zhao, Y. Highly Conductive Nanograting−Nanohole Structures with Tunable and Dual-Band Spectral Transparency. *ACS Appl. Electron. Mater.* **2021**, *3*, 3489−3500.

(21) Ingram, W. M.; Han, C.; Zhang, Q.; Zhao, Y. Optimization of Ag-Coated Polystyrene Nanosphere Substrates for Quantitative Surface-Enhanced Raman Spectroscopy Analysis. *J. Phys. Chem. C* **2015**, *119*, 27639−27648.

(22) Han, C.; Ye, D.; Zhao, Y.; Fu, J.Physical vapor deposition of Ag nanoparticles through shadowing and re-emission effects. *J. Vac. Sci. Technol.***2018**, *36*(). DOI: 10.1116/1.5026581.

(23) Bradley, L.; Ye, D.; Luong, H. M.; Zhao, Y. Transition from discrete patches to plasmonic nanohole array by glancing angle deposition on nanosphere monolayers. *Nanotechnology* **2020**, *31*, 205301.

(24) Whitney, I.*The Fabrication and Application of Plasmonic Nanostrucures Fabricated by Nanosphere Lithography*; University of Georgia, 2016.

(25) Ye, D. X.; Lu, T. M.Ballistic aggregation on two-dimensional arrays of seeds with oblique incident flux: Growth model for amorphous Si on Si. *Phys. Rev. B***2007**, *76*(). DOI: 10.1103/PhysRevB.76.235402.

(26) (a) Karabacak, T.; Singh, J. P.; Zhao, Y. P.; Wang, G. C.; Lu, T. M. Scaling during shadowing growth of isolated nanocolumns. *Phys. Rev. B* **2003**, *68*, 125408. (b) Ye, D.; Zhao, Y.; Fu, J. HanPhysical vapor deposition of Ag nanoparticles through shadowing and re-emission effects. *J. Vac. Sci. Technol.* **2018**, *36*, 051802.

(27) Palik, E. D.*Handbook of Optical Constants of Solids*; Academic Press, 1985.

(28) Hawkeye, M. M.; Taschuk, M. T.; Brett, M. J.*Glancing Angle Deposition of Thin Films_Engineering the Nanoscale*; WILEY, 2014.

(29) Bradley, L.; Zhao, Y. Uniform Plasmonic Response of Colloidal Ag Patchy Particles Prepared by Swinging Oblique Angle Deposition. *Langmuir* **2016**, *32*, 4969−4974.

(30) Lee, S. H.; Bantz, K. C.; Lindquist, N. C.; Oh, S.-H.; Haynes, C. L. Self-Assembled Plasmonic Nanohole Arrays. *Langmuir* **2009**, *25*, 13685−13693.

(31) (a) Carlson, D.; Ai, B.; Zhao, Y. LarsonThe extraordinary optical transmission and sensing properties of Ag/Ti composite nanohole arrays10.1039/C8CP07729K. *Phys. Chem. Chem. Phys.* **2019**, *21*, 3771−3780. (b) Wang, Y.; Yang, F.; Zhang, Z.; Zhao, Y. Performance of Transparent Metallic Thin Films. *J. Phys. Chem. C* **2021**, *125*, 16334−16342.

(32) (a) Chan, G. H.; Zhao, J.; Hicks, E. M.; Schatz, G. C.; Van Duyne, R. P. Plasmonic Properties of Copper Nanoparticles Fabricated by Nanosphere Lithography. *Nano Lett.* **2007**, *7*, 1947−1952. (b) Chan, G. H.; Zhao, J.; Schatz, G. C.; Van Duyne, R. P. Localized Surface Plasmon Resonance Spectroscopy of Triangular Aluminum Nanoparticles. *J. Phys. Chem. C* **2008**, *112*, 13958−13963.

(33) Wang, Y.; Zhang, Z.; Zhao, Y. The effect of nanorod position on the plasmonic properties of the complex nanorod in nanohole arrays. *J. Phys. D: Appl. Phys.* **2021**, *54*, 155201.

(34) Wood, R. W. Anomalous Diffraction Gratings. *Phys. Rev.* **1935**, *48*, 928−936.

(35) Zhao, Y.-P.; Wang, G.-C.; Lu, T.-M.*Characterization of Amorphous and Crystalline Rough Surface - Principles and Applications*; Academic Press, 2001.

(36) Yang, H. N.; Zhao, Y. P.; Chan, A.; Lu, T. M.; Wang, G. C. Sampling-induced hidden cycles in correlated random rough surfaces. *Phys. Rev. B* **1997**, *56*, 4224−4232.